The following publication Chen, L., Mak, C. M., Hang, J., & Dai, Y. (2024). Influence of elevated walkways on outdoor thermal comfort in hot-humid climates based on on-site measurement and CFD modeling. Sustainable Cities and Society, 100, 105048 is available at https://doi.org/10.1016/j.scs.2023.105048.

Influence of elevated walkways on outdoor thermal comfort in hot-humid climates based on on-site measurement and CFD modeling

Abstract

The elevated walkway is commonly designed to facilitate pedestrian movement and alleviate traffic conflicts. Its shading effect is supposed to benefit outdoor thermal comfort on hot days, especially in hot and humid regions, but relevant research has been scarce. To validate this hypothesis, we conducted on-site measurements on an elevated walkway and ground sidewalks in Hong Kong during summer and winter. Then parametric simulation study was performed to investigate the effects of the elevated walkway, street aspect ratio (*H/W*), walkway width (W_{ew}), and sidewall type on outdoor thermal comfort in ideal urban street canyons through large eddy simulation and RayMan modeling. Results indicate that the elevated walkway increases the ground-level physiological equivalent temperature (PET) by up to 2.7 ℃ and causes a 2−17 ℃ lower walkway-level PET value. Ground-level and walkway-level PET values initially increase and then decrease with rising *H/W* but positively correlate with W_{ew}. Compared to the open sidewall, the semi-hermetic sidewall decreases the ground-level PET value slightly (below 0.8 ℃) but raises the walkway-level PET value (below 1.3 ℃). This study confirms the efficacy of elevated walkways in improving pedestrian thermal comfort in hot weather, contributing to shade strategies for heat stress mitigation and thermal comfort improvement.

Keywords: Outdoor thermal comfort, Shading strategy, Elevated walkway, Computational fluid dynamics, Street aspect ratio

1. Introduction

High temperatures and heat waves have become more frequent and intense than ever due to global warming and the urban heat island effect (Perkins-Kirkpatrick and Lewis, 2020). In 2022, many European countries experienced the hottest summer on record and several severe heatwaves (C3S, 2022), and China also reported its record-breaking regional heatwaves during summer (Jiang et al., 2023). The sweltering weather seriously impairs outdoor thermal comfort and increases the risk of heat stress, badly affecting city dwellers' daily lives and production. Given this worrying situation, cities are in urgent need of effective strategies to improve outdoor thermal comfort on hot days, particularly in hot and humid regions.

Lai et al. (2019) summarized four mitigation strategies for improving local thermal environments: modifying urban geometry, growing vegetation, utilizing reflective surfaces, and building water bodies. These cooling strategies take effect mainly by means of reducing thermal radiation, cooling the air, or accelerating air currents. As the cooling effect of passive strategies on outdoor air temperature is usually limited (Lai et al., 2019), thermal comfort improvement is achieved primarily through changing thermal radiation and wind velocity (Niu et al., 2015). Furthermore, many studies found that thermal radiation contributes more to outdoor human thermal perception than wind velocity, suggesting the crucial role of shade in reducing heat stress (Aleksandrowicz and Pearlmutter, 2023; Ali-Toudert and Mayer, 2007; Lai et al., 2020; Xu et al., 2018). The shade is shielded from exposure to direct sunlight, providing a more thermally comfortable environment on hot days than the sun-exposed area (Lin et al., 2013).

Various shading elements, natural, engineered, or building-related, have been documented to improve outdoor thermal comfort effectively across different climate regions (Aleksandrowicz and Pearlmutter, 2023; Lai et al., 2023; Li et al., 2022c; Rossi et al., 2022; Talebsafa et al., 2023; Yang et al., 2023). Urban tree planting is a widely used, nature-based

shading strategy, but its application is subject to the growing space, climate, soil, irrigation condition, and maintenance cost (Middel et al., 2021). In contrast, engineered shading methods, such as umbrellas (Lee et al., 2018), sun sails (Elgheznawy and Eltarabily, 2021; Kántor et al., 2018), pergolas (Watanabe et al., 2014), pavilions (Niu et al., 2020), and canopies (Palomo Amores et al., 2023), are more flexible and convenient. These shading devices are easily removed when shade is undesired. Building-related shade is land-saving and generally provided by particular urban forms, including overhangs (Crewe et al., 2016; Middel et al., 2021), street canyons (Nasrollahi et al., 2021), arcades (Tan et al., 2022; Yin et al., 2022), covered passageways (Yıldırım, 2020), and elevated buildings (Du et al., 2017; Huang et al., 2017). Table 1 summarizes the main findings of previous studies on shading strategies.

Table 1 Overview of studies on shading strategies related to outdoor thermal comfort. (T_a: air temperature; RH: relative humidity; PET: physiological equivalent temperature; PMV: predict mean vote; T_s: surface temperature; TSV: thermal sensation vote; UTCI: universal thermal climate index; ETU: universal effective temperature.)

Reference	Climate/Location	Shade type	Main findings
Lai et al. (2023)	Humid-subtropical (Cfa) Shanghai, China	Tree	The differences in T_a and RH are no more than 1 ℃ and 0.8 g/kg among different tree layouts; tree shade decreases T_{mrt} and PET by up to 20 ℃ and 11 ℃.
Palomo Amores et al. (2023)	Hot-summer Mediterranean (Csa) Seville, Spain	Tree Canopy	The fully grown trees scenario and incorporation of slat structures and small trees scenario decrease daily discomfort hours by 32% and 21%, respectively.
Mahmoud and Abdallah (2022)	Hot-arid (Bwh) New Assiut, Egypt	Tree Canopy	The hybrid of trees with orthogonal (or diagonal) staggered wood canopies can reduce T_a and PET by up to 6.08 (5.8) ℃ and 18.5 (18.6) ℃ in a wide canyon.

Elgheznawy and Eltarabily (2021)	Subtropical hot-arid (Bwh) Port Said, Egypt	Sun sail	When the coverage ratio of sun sails in the school courtyard is 60% or more, T_a, PMV, and PET can decrease around 0.5 ℃, over 0.6 ℃, and above 4 ℃, respectively.
Middel et al. (2021)	Hot-arid (Bwh) Tempe, USA	Tree Engineered Building	Building shades (overhangs, arcade, tunnel, and street canyon) provide the maximum T_s and T_{mrt} reduction in the daytime, followed by trees and engineered shades (umbrella, sun sail, canopy, and pergolas).
Niu et al. (2020)	Monsoon-influenced humid subtropical (Cwa) Xi'an, China	Tree Pavilion	Taking activities under tree or pavilion shade causes lower mean skin temperature and TSV than in unshaded open areas.
Lee et al. (2020)	Monsoon-influenced humid subtropical (Cwa) Hong Kong, China	Canopy	The shaded zone cools T_a, PET, and UTCI by up to 0.8 ℃, 8.2 ℃, and 5.3 ℃, respectively, compared to the sun-exposed zone.
Yin et al. (2019)	Monsoon-influenced humid subtropical (Cwa) Guangzhou, China	Tree Arcade Street canyon	Tree streets show stronger cooling effects on thermal stress than arcade streets when the streets are north-south oriented; both tree and arcade streets perform the best at the east-west orientation.
Lee et al. (2018)	Warm-summer humid continental (Dfb) London, Canada	Tree Building Umbrella	The building shade (wall and overhang) is the most effective, followed by the tree and umbrella shades.
Cheung and Jim (2018)	Monsoon-influenced humid subtropical (Cwa) Hong Kong, China	Tree Shelter	The tree shade has significantly stronger cooling effects on T_a and UTCI than the shelter shade throughout the day; the tree shade causes a higher reduction in PET than the shelter shade, insignificant in the daytime and significant in the nighttime.

Kántor et al. (2018)	Humid-subtropical (Cfa) Pécs, Hungary	Tree Sun sail	The small trees and low-hanging sun sails reduce PET by 9 ℃ and 5.8 ℃; dense-canopy trees and high-hanging sun sails reduce PET by over 10 ℃.
Watanabe et al. (2014)	Humid-subtropical (Cfa) Nagoya, Japan	Pergola Building	In sunny weather, the building and pergola shades decrease ETU by 18.4 ℃ and 16.2 ℃; in cloudy weather, the reductions in ETU are 9.3 ℃ and 6.8 ℃, respectively.

With the city population burgeoning, the elevated walkway has become prevalent in high-density cities to ameliorate pedestrian walkability, relieve ground traffic, and alleviate traffic conflicts between pedestrians and vehicles (Highways Department, 2022). As one of the most densely populated areas in the world, Hong Kong has over one thousand elevated walkways (Highways Department, 2022). Beyond traditional functions, the elevated walkway networks of Hong Kong promote multi-layer economic activities and provide public relaxing places (Rotmeyer, 2006). Undoubtedly, elevated walkways have been a part of city dwellers' daily routines. As shown in Fig. 1, the elevated walkway usually has a cover or canopy to shield pedestrians against the sunshine and precipitation. Analogous to other shading elements, this canopy structure is expected to mitigate heat stress on pedestrians by reducing incoming solar radiation and cooling the surface temperature. However, to the authors' best knowledge, outdoor thermal comfort research on the elevated walkway is almost vacant, leading to the conceptualization of this study. Yang et al. (2016) found that the open elevated walkway provides worse thermal comfort than the shaded ground sidewalk in summer in a subtropically hot and humid city, which does not apply to the covered elevated walkway. Furthermore, previous studies demonstrated that the elevated walkway decreases mean wind velocity near the ground (Chen et al., 2023; Duan et al., 2020). This phenomenon raises another new issue: how do elevated walkways influence outdoor thermal comfort on the ground sidewalk?

Fig. 1. Some elevated walkways in Hong Kong photographed by authors.

Therefore, this study aims to explore the impacts of elevated walkways on outdoor thermal comfort. PET was employed to characterize levels of thermal stress and thermal comfort. We carried out on-site measurements on and underneath an elevated walkway on sunny summer and winter days in Hong Kong to compare the thermal environment of the elevated walkway with the ground sidewalk. Further, we designed ideal urban street canyon and elevated walkway models to investigate outdoor thermal comfort under different scenarios by computational fluid dynamics (CFD) simulation and Rayman modeling. The outcome of this study will fill the knowledge gap on outdoor thermal comfort around elevated walkways, facilitating the development of livable cities.

2. Materials and methods

As depicted in Fig. 2, this study consisted of on-site measurements on an authentic elevated walkway in Hong Kong and numerical simulations on the ideal urban street canyon. T_a, RH, the globe temperature (T_g), and wind velocity (v) on the elevated walkway and ground sidewalks were recorded during the measurements. T_{mrt} was calculated from T_a, v, and T_g. Inputing these parameters, personal data, clothing, and activity to RayMan Pro 3.1, PET could be yielded. Regarding ideal urban street canyons, large eddy simulation (LES) was employed to simulate mean wind velocity data. Simulated v data were then converted into in-situs v data. Based on in-situs v data, sky view factors (SVF) estimated by SkyHelio, date and time, geographic and personal data, clothing and activity, cloud amount, and T_a and RH from the

Hong Kong Observatory, T_{mrt} and PET could be calculated by RayMan Pro 3.1. The impacts of the elevated walkway, street aspect ratio (H/W), walkway width (W_{ew}), and sidewall type (or height, h_{sw}) on thermal comfort were investigated.

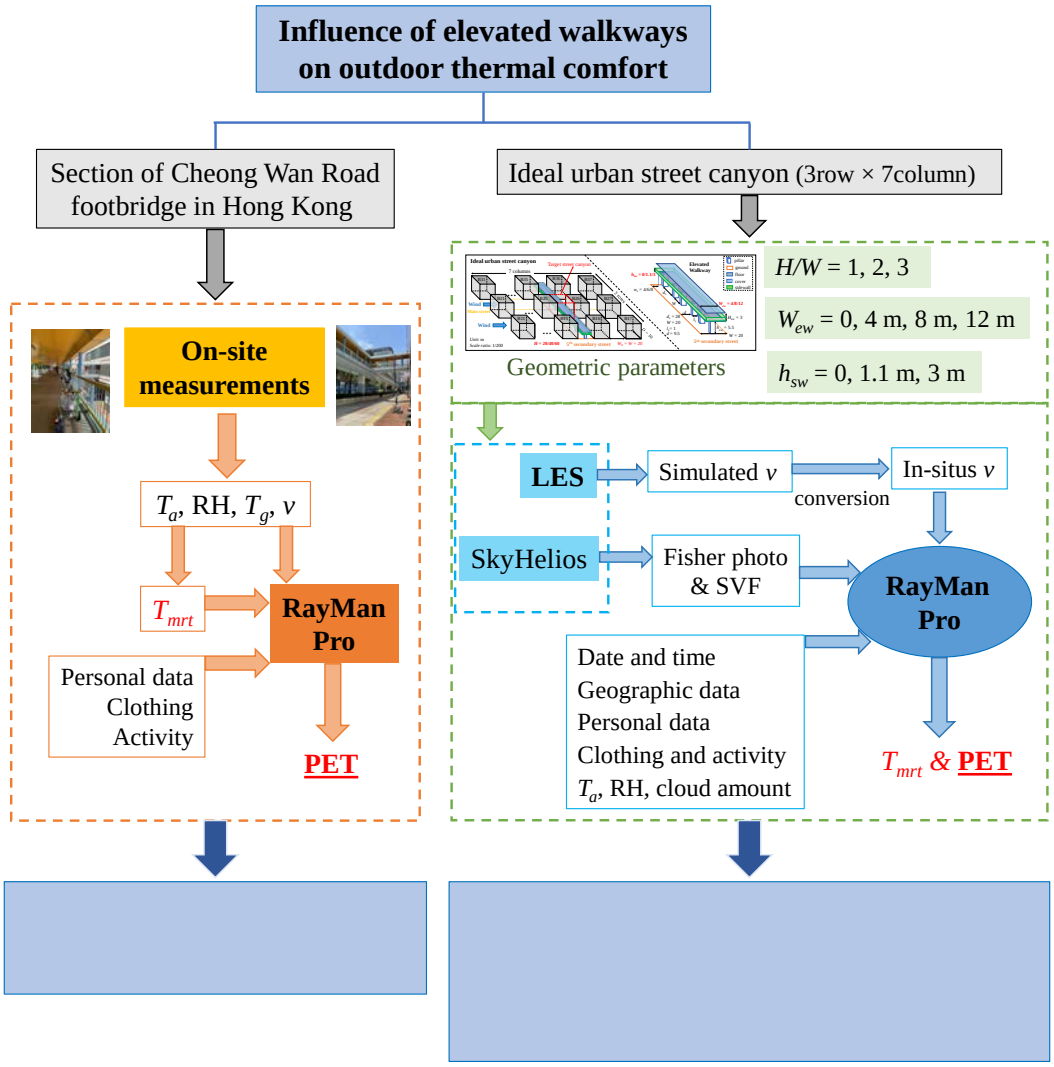

Fig. 2. The flow chart of methodology.

2.1. Study area

Hong Kong (22°08'N−22°35'N, 113°49'E−114°31'E) lies on the southern coast of China, encircled by the South China Sea on the east, west, and south sides. According to the Köppen-Geiger climate classification (Kottek, 2006), Hong Kong has a monsoon-influenced humid subtropical climate (Cwa), with nearly 80% of the annual rainfall occurring during the summer

monsoon (Hong Kong Observatory, n.d.-b). Therefore, summers are intensely hot and humid, whereas winters are cool to mild and relatively dry. Table A.1 shows that the climatological normals (1991−2020) of daily mean temperatures are ~28.0°C between May and September and ~17.3°C from December to February, with an RH of 60−80% (Hong Kong Observatory, n.d.-b). The prevailing wind at the Hong Kong Observatory, about 500 m from the study area, is from the west during June to August and from the east over the remaining months, with monthly average mean wind velocity from 2.5 m/s to 3.1 m/s (Hong Kong Observatory, n.d.-b). The Waglan Island weather station, a remote observation site at the southeast tip of Hong Kong, shows that its prevailing wind is from the southwest (5.2−6 m/s) during June to August and from the north to east (5.9−7.4 m/s) over the remaining months (Hong Kong Observatory, n.d.-b). In contrast to Waglan Island, the Hong Kong Observatory has a steadier wind velocity, influenced little by wind direction.

The measured elevated walkway is a section of Cheong Wan Road Footbridge in East Tsim Sha Tsui, Yau Tsim Mong District, Hong Kong. Yau Tsim Mong District is one of the major centers of commercial activities and traffic arteries in Hong Kong, with dense population and heavy traffic. According to the local climate zone (LCZ) classification map of Hong Kong (Zheng et al., 2018), the study area belongs to high-rise LCZs. Fig. 3(a) displays the location and surroundings of the study area (marked in red star). The Cheong Wan Road Footbridge is located at one of the most congested roads in Hong Kong, connecting a mass transit railway station, a university campus, and the Cross Harbour Tunnel bus stop. The measured section is above the two-way, four-lane science museum path, between a fifteen-story commercial center and a twenty-eight-story hotel. The measured section extends from west-southwest to east-northeast, ~7.5 m from the nearest fifteen-story building. The walkway is ~5.6 m above the ground, with a cover and two-row railings of 1.1 m high. And the interior for pedestrians moving is ~4.8 m wide and ~2.5 m high. The position of four monitoring sites is shown in Fig.

3(b). Sites E1 and E2 are on the elevated walkway, while Sites S1 and S2 are on the ground sidewalk.

Fig. 3. (a) Location and surroundings of the study area; (b) positions of monitoring sites and the mobile weather station used during on-site measurements.

2.2. On-site measurement

A mobile weather station equipped with temperature and relative humidity sensors, an ultrasonic anemometer, and a 75 mm black globe thermometer was used to record meteorological parameters. These instruments were fixed orderly at a baby carriage, 1.1 m to

1.5 m above the ground or walkway floor. The sampling frequency for T_a, RH, and v was 20 Hz, while T_g was recorded every second. Table 2 summarizes the equipment specifications. During the measurements, the working mobile weather station alternately collected meteorological parameters at the elevated walkway and ground sidewalk. Each place acquired two to five rounds of measurements. And the stay duration at one place was mainly 30 to 40 minutes for each round. Owing to the shading from surrounding buildings, the sunlight exposure duration of Sites S1 and S2 varied regularly. Thus, the daily experiment period was when the ground sidewalk was exposed to direct sunlight. The alternate sequences were set partly with the constraint of sunlight exposure duration and sometimes reversed between adjacent experimental dates to minimize the potential effects of alternate sequences on data. Experiment dates and duration, alternate sequences, and daily weather conditions during experiment days are presented in Table 3. The on-site measurements were conducted on twelve sunny days in August, September 2022, and January 2023, during which the Hong Kong Observatory issued eight "very hot" and three "cold" weather warnings. So, this study covered the hot and cold days of Hong Kong.

Table 2 Summary of equipment specifications.

Meteorological parameter	Equipment model	Measurement range	Accuracy
T_a	R.M.YOUNG 41382	−50−50 ℃	±0.3 ℃
RH	R.M.YOUNG 41382	0−100 %	±1 %
v	R.M.YOUNG 81000	0−40 m/s	±0.05 m/s
T_g	WBGT-2010SD	0−80 ℃	±0.6 ℃

Table 3 Experiment date and duration, alternate sequences, and daily weather conditions at the Hong Kong Observatory during experiment periods (Hong Kong Observatory, n.d.-a). T_{max} and T_{min} denote the daily maximum and minimum air temperatures, respectively.

Date (dd/mm/yyyy)	Duration (HH: mm)	Alternate sequence	T_{max} (°C)	T_a (°C)	T_{min} (°C)	RH (%)	Cloud Amount (%)	Warning Information
23/08/2022	11:20−14:00	S1→E1→S1	34.5	31.1	28.6	77	28	Very hot
27/08/2022	10:10−15:00	S2→E2→S2	33.0	29.7	27.4	78	60	Very hot
28/08/2022	10:00−11:00	E2→S2	34.4	30.5	28.3	80	57	Very hot
	13:00−17:00	S2→E2→S2						
03/09/2022	10:00−16:30	S2→E2→S2	33.9	30.0	26.9	54	30	Very hot
04/09/2022	09:30−16:00	S2→E2→S2	34.7	30.8	27.7	55	26	Very hot
05/09/2022	10:00−14:00	S1→E1→S1	35.3	31.1	28.8	52	38	Very hot
06/09/2022	10:00−14:30	E1→S1→E1	34.5	30.8	28.4	61	51	Very hot
16/09/2022	10:00−14:00	E1→S1→E1	33.8	30.8	28.6	63	36	Very hot
18/01/2023	10:00−12:00	E1→S2→E1	17.1	14.3	11.5	58	41	Cold
	12:30−16:20	S1→E1→S1						
19/01/2023	09:40−12:20	S2→E1→S2	18.7	16.1	13.3	63	23	-
	12:20−16:20	S1→E1→S1						
28/01/2023	09:40−12:20	S2→E1→S2	15.7	12.9	10.6	28	20	Cold
	12:20−15:30	E1→S1→E1						
29/01/2023	09:40−12:10	S2→E1→S2	16.0	12.8	9.8	35	1	Cold
	12:10−15:30	S1→E1→S1						

2.3. CFD simulation

2.3.1. Cases description

CFD simulations were conducted to further understand the impacts of street aspect ratio and walkway dimensions on outdoor thermal comfort as complements to on-site measurements.

The ideal urban street canyon model was designed according to Leitl and Schatzmann (2010), which comprised three-row and seven-column generic buildings scaled down by 200 in CFD simulations. Fig. 4(a and b) illustrates the schematic drawings and geometric dimensions. The building model was tagged with B, row, and column for description. No-walkway and walkway models differed in whether an elevated walkway was constructed at the fifth secondary street (marked in blue). The elevated walkway was simplified from actual prototypes, reserving primary structures of cover, floor, sidewalls, and supporting pillars but ignoring some details such as elevators, stairways, and handrails. The target street between B25 and B26 (marked in red) was selected for research, for it was surrounded by obstacles and under the most unfavorable wind condition. Changing building height (H) with a constant street width (W) acquired three street aspect ratios of H/W = 1, 2, and 3. The narrow, middle, and wide walkways were defined with walkway widths (W_{ew}) of 4 m, 8 m, and 12 m. This study classified sidewalls into open (h_{sw} = 0), semi-hermetic (h_{sw} = 1.1 m), and hermetic types (h_{sw} = H_{ew} = 3 m) according to air permeability. Expressly, open sidewalls (OP-Wall) referred to well-ventilated railings, while semi-hermetic (SH-Wall) and hermetic (H-Wall) sidewalls represented unventilated concrete or glass barriers (see Fig.1). The basic walkway case had settings of H/W = 1, W_{ew} = 8 m, and h_{sw} = 0.

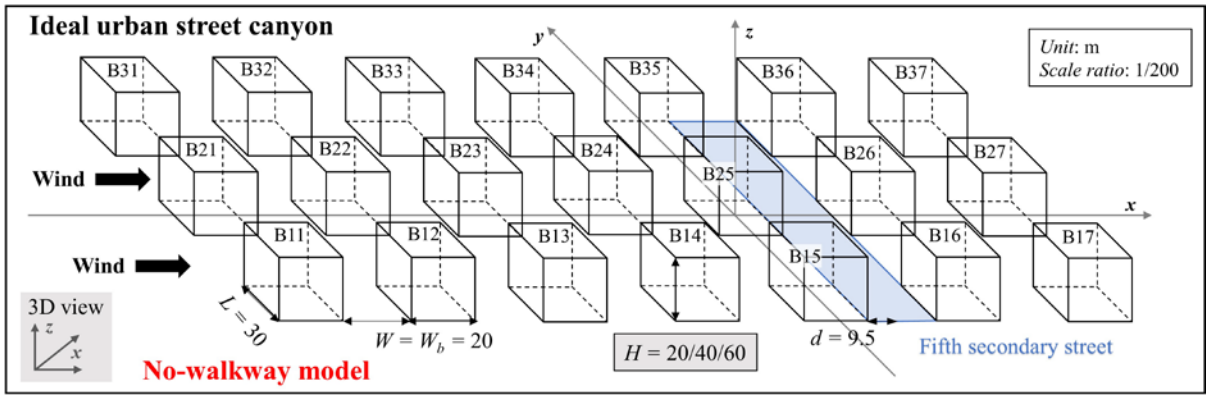

(a)

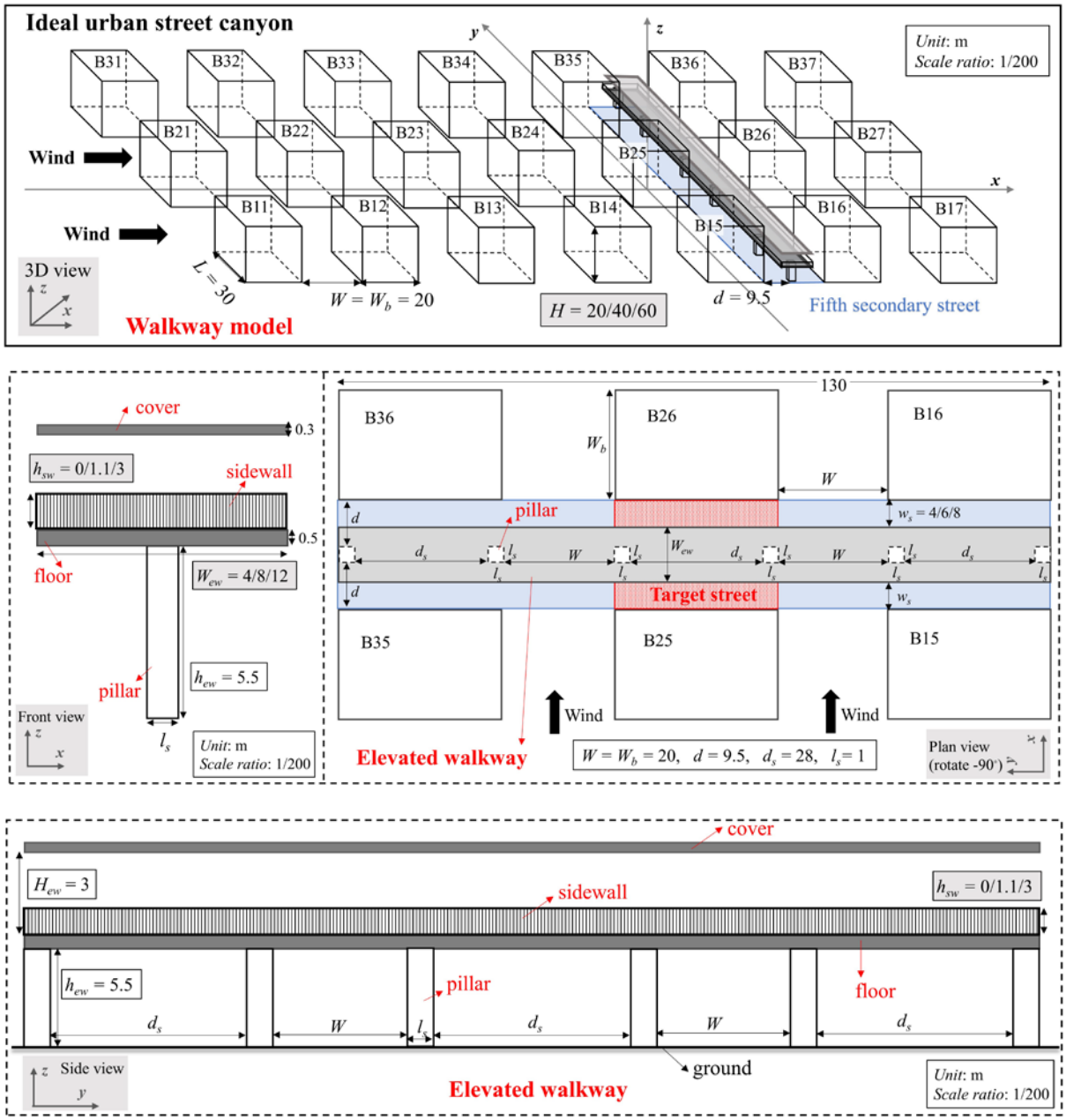
Ideal urban street canyon
Unit: m
Scale ratio: 1/200
Wind
Wind
B31
B32
B33
B34
B35
B36
B37
B21
B22
B23
B24
B25
B26
B27
B11
B12
B13
B14
B15
B16
B17
3D view
L = 30
W = W_b = 20
H = 20/40/60
d = 9.5
Fifth secondary street
Walkway model
cover
0.3
h_sw = 0/1.1/3
sidewall
0.5
floor
W_ew = 4/8/12
pillar
h_ew = 5.5
l_s
Front view
Unit: m
Scale ratio: 1/200
130
B36
B26
B16
W_b
W
d
pillar
w_s = 4/6/8
d_s
l_s
W
W_ew
Target street
B35
B25
B15
Wind
Wind
Elevated walkway
W = W_b = 20, d = 9.5, d_s = 28, l_s = 1
Plan view
(rotate -90°)
cover
H_ew = 3
sidewall
h_sw = 0/1.1/3
h_ew = 5.5
pillar
floor
d_s
W
l_s
ground
Side view
Elevated walkway
Unit: m
Scale ratio: 1/200

(b)

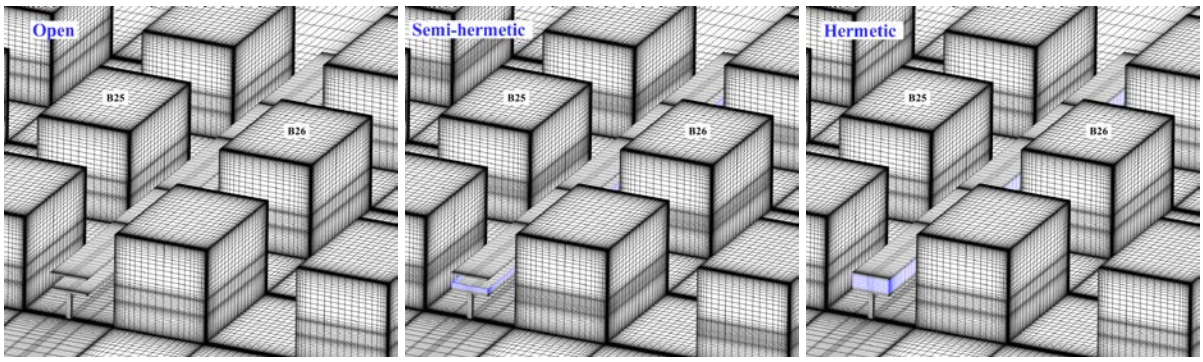
Open
Semi-hermetic
Hermetic
B25
B26

(c)

Fig. 4. Schematic drawings and geometric dimensions of ideal urban street canyon models: (a) no-walkway and (b) walkway. (c) Grid arrangements for three walkway cases: open, semi-hermetic, and hermetic sidewall conditions.

2.3.2. Computational domain, boundary conditions, and solution method

According to the best practice guidelines (Franke et al., 2007; Tominaga et al., 2008), the computational domain was developed with upstream, downstream, lateral, and top lengths of 5*H*, 15*H*, 5*H*, and 5*H*, respectively. The domain was discretized into millions of structured hexahedral grids with a minimum grid size of 0. 5 mm (on a reduced scale) (Chen et al., 2023; Dai et al., 2018). Examples of grid arrangements are shown in Fig. 4(c). The domain inlet was specified as the velocity-inlet boundary. The fitting profiles for inlet wind velocity (*U*), turbulent kinetic energy (*k*), and turbulent dissipation rate (ε) obtained from wind-tunnel data (Leitl and Schatzmann, 2010) were expressed in Eqs. (1−3), where $u^* = 0.374$ m/s was the friction velocity, $z_0 = 0.00075$ m was the roughness length, and $C_1 = 0.025$, $C_2 = 0.41$ and $C_\mu^* = 0.069$ were equation constants (Ai and Mak, 2015). Pressure-outlet boundary condition with zero static pressure was applied at the domain outlet. Normal velocity and normal gradients of all variables were set to zero at the domain top and lateral boundaries. All solid surfaces were defined as no-slip walls.

$$U = \frac{u^*}{\kappa} ln(\frac{z+z_0}{z_0}) \tag{1}$$

$$k = \sqrt{C_1 ln(z+z_0) + C_2} \tag{2}$$

$$\varepsilon = \frac{u^* \sqrt{C_\mu^*}}{\kappa(z+z_0)} \sqrt{C_1 ln(z+z_0) + C_2} \tag{3}$$

All CFD simulations were completed in ANSYS Fluent 19.0 (2018) on the Tianhe II supercomputer of the National Supercomputer Center in Guangzhou, China. The finite volume

scheme was employed for discretizing fluid governing equations. The steady RNG k-ε model with enhanced wall treatments simulated initial flow fields for LES. The initial steady simulations adopted the SIMPLEC algorithm as the pressure-velocity coupling scheme and second-order-accurate upwind and central-differential methods for convection and diffusion terms. The residuals for equations were set to 10^{-4}. In LES, this study selected the Smagorinsky−Lilly model as the subgrid-scale model and the PISO algorithm as the pressure-velocity coupling scheme. The bounded central-differencing scheme and second-order implicit formulation were used for spatial and temporal terms. The vortex method with 190 vortices was used to add turbulent fluctuations to the inlet mean velocity profile (Dai et al., 2018; Fluent, 2013). The time step size and data sampling length for data statistics were set to 0.005 s and 12 s, respectively (Dai et al., 2018). The convergence for each iteration was considered to be reached when monitoring variables were stable for several iterations.

2.3.3. Validation study

Wind tunnel experiments by Leitl and Schatzmann (2010) were applied to validate the performance of described CFD methods for modeling the mean flow in an urban street canyon. The ideal urban street canyon resembled the no-walkway model, with H/W = 1.25. All CFD setups for simulating the validation case were consistent with Section 2.3.2, except the domain lateral length followed the wind tunnel width. Distributions of wind tunnel and LES modeling normalized mean wind velocity (U_{xy}/U_{ref}) on the horizontal plane of z = 0.0625 m (on a reduced scale) are displayed in Fig. 5, where U_{ref} is the reference velocity of the approaching flow at z = 0.66 m. It can be observed that curves of LES results are either through or very close to circles of wind tunnel data. Moreover, the fraction of predictions within a factor of two of observations (FAC2), the fraction bias (FB), and the normalized mean square error (NMSE) for wind-tunnel data and LES results were 0.98, 0.12, and 0.03, respectively. These validation metrics meet the recommended requirements for acceptable model performance, namely FAC2 >

0.5, |FB| < 0.3, and NMSE < 4 (Hanna et al., 2004; Sabatino et al., 2011; Schatzmann M, 2010). The validation results demonstrate that the CFD method in Section 2.3.2 can predict a satisfactory mean flow field in an ideal urban street canyon. Chen et al. (2023) and Dai et al. (2018) describe more detailed information on this validation study.

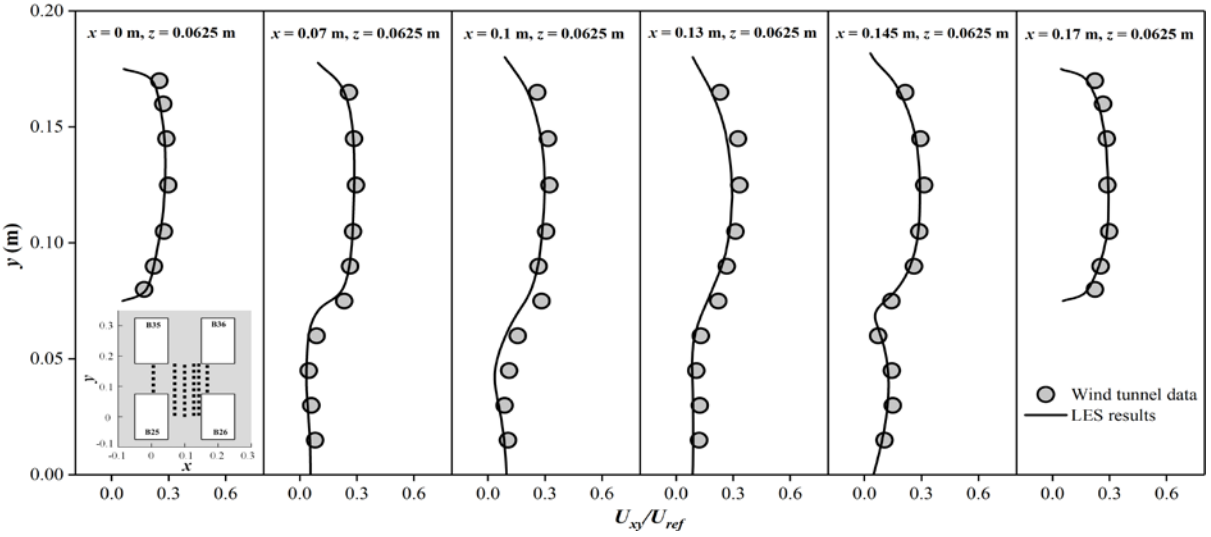

Fig. 5. Comparison of U_{xy}/U_{ref} distribution on the horizontal plane between wind tunnel experiments and LES. Dash lines in the first diagram indicate the measuring positions.

2.4. Thermal comfort assessment

2.4.1. Mean radiant temperature (T_{mrt})

T_{mrt} is defined as the uniform temperature of an imaginary perfect blackbody in which the human body exchanges the equivalent radiant heat as in an assessed environment (ASHRAE, 2017). There are several well-recognized methods to estimate T_{mrt}. Utilizing the black globe thermometer and temperature and humidity sensors is a simple and economical way, by which T_{mrt} is calculated from T_g, T_a, v, globe diameter (D, m), and emissivity (ε = 0.95) (see Eq. (4)) (ASHRAE, 2017). The most accurate method for determining T_{mrt} is using six-directional (i.e., up, down, east, west, south, and north) radiation fluxes and correlative angular factors (F_i) (Höppe, 1992). As shown in Eq. (5), K_i and L_i are short- and long-wave radiation flux densities; α_k = 0.7 and α_l = 0.97 are absorption coefficients for short- and long-wave radiation; ε_p = α_l

represents the emissivity of the human body; and σ = 5.67×10^{-8} Wm^{-2}K^{-4} is the Stefan–Boltzmann constant (Höppe, 1992). However, measuring radiation flux densities with net radiometers is expensive and complex. Apart from the above measurement methods, T_{mrt} can be simulated by the RayMan model (Li et al., 2023; Li et al., 2020; Zhong et al., 2023). This model simulates radiation fluxes according to the date and time, latitude and longitude, altitude, time zone, albedo and emissivity of solid surfaces, geometrical features of buildings and vegetation, SVF, T_a, RH, and cloud cover in octaves (Matzarakis, 2007, 2010).

$$T_{mrt} = \left[\left(T_g + 273.15\right)^4 + \frac{1.10\times10^8\times v^{0.6}\times(T_g - T_a)}{\varepsilon D^{0.4}}\right]^{0.25} - 273.15 \quad (4)$$

$$T_{mrt} = \left(\frac{\sum_{i=1}^{6} F_i\times(\alpha_k K_i + \alpha_l L_i)}{\varepsilon_p \sigma}\right)^{0.25} - 273.15 \quad (5)$$

This study employed the black globe thermometer rather than net radiometers during on-site measurements because the former was more mobile and occupied less space. Li et al. (2022a) have developed the correlation function (see Eq. (6)) of two T_{mrt} from simultaneously measuring T_g (a 75 mm WBGT-2010SD globe thermometer) and six-directional radiation flux densities (three Kipp & Zone CNR4 net radiometers). Therefore, for T_{mrt} on the actual elevated walkway and ground sidewalk, this study computed T_{mrt} (T_g) from Eq. (4) first, then corrected the initial results to T_{mrt} (*six-direcitonal*) with Eq. (6) (Kántor et al., 2014; Lam et al., 2021; Li et al., 2022a; Li et al., 2022b).

$$T_{mrt}(six - directional) = (T_{mrt}(T_g) + 3.6986)/1.1386 \quad (6)$$

As LES only provided wind velocity data for ideal urban street canyon models, T_{mrt} was modeled using RayMan Pro 3.1. Fisheye images and SVF of interest points on the ground sidewalk and elevated walkway were obtained from the SkyHelio model (Matzarakis and Matuschek, 2011). In line with on-site measurements, the parametric simulation study specified that the geographic latitude and longitude were 22°18'N and 114°10'E, and the dates were 23

August and 28 January. The modeling weather was sunny without clouds. The local time was set as LST 12: 30 to ensure two-side ground sidewalks were exposed to direct sunlight. The monthly average T_{max} and RH of August and January were adopted as input T_a and RH for ground sidewalks. According to on-site measurements, elevated walkways were assumed to have 1°C lower T_a and 3% higher *RH* than ground sidewalks in ideal urban street models. Detailed geographic and meteorological input parameters for the RayMan model are enumerated in Table 4.

Table 4 Geographic, meteorological, and personal information for modeling T_{mrt} and calculating PET (ASHRAE, 2013; Hong Kong Observatory, n.d.-b; ISO 9920:2007, 2007).

Season	Summer	Winter
Date (dd/mm/yyyy)	23/08/2022	28/01/2023
LST (HH: mm)	12: 30	12: 30
T_a (°C)	SW: 31.3, EW: 30.3	SW: 18.7, EW: 17.7
RH (%)	SW: 74, EW: 77	SW: 67, EW: 70
Cloud amount (%)	0 (Sunny)	0 (Sunny)
Clothing (clo)	0.4 (Short-sleeve shirt, light-weight trousers)	0.9 (long-sleeve shirt, jacket, trousers)
Sex, Age, Height, Weight	Male, 25 years old, 1.75 m, 70 kg	
Activity	100 W (Walking about)	
Location	East Tsim Sha Tsui, Hong Kong (22°18'N, 114°10'E)	

2.4.2. Physiological equivalent temperature (PET)

As the most widely used index in outdoor thermal comfort, PET is defined as the air temperature at which the human body reaches a heat budget balance under an indoor condition of no wind and solar radiation with skin and core temperatures identical to those under the assessed outdoor environment (Höppe, 1999; Kumar and Sharma, 2020). This index indicates

the integral thermal stress of the outdoor environment on the human body with a universal Celsius temperature unit, which is readily comprehensible for ordinary people without knowledge of human thermal biometeorology (Höppe, 1999). Therefore, this study applied PET to quantify pedestrian thermal stress and thermal comfort on ground sidewalks and elevated walkways.

All calculations of PET were completed in RayMan Pro 3.1. The personal data, clothing insulation, and activity level are shown in Table 4. For actual sites, PET was calculated from measured meteorological data. Regarding ideal urban street canyon models, the settings of T_a, RH, and modeling T_{mrt} are elaborated in Section 2.4.1. As for v, the simulated wind velocity ($v_{ped,\ cfd}$) required conversion into in-situs velocity ($v_{ped,\ situ}$) before being input to RayMan Pro 3.1. In Eq. (7), $v_{ref,\ situ}$ = 6.4 m/s is the mean wind velocity at Waglan Island, and $v_{ref,\ cfd}$ = 5.6 m/s is the approaching flow's mean velocity at the same scale height in LES. The anemometer at the Waglan Island weather station is 83 m above mean sea level.

$$\frac{v_{ped,cfd}}{v_{ref,cfd}} = \frac{v_{ped,situ}}{v_{ref,situ}} \tag{7}$$

3. Results

3.1. On-site measured results of Cheong Wan Road footbridge

During the measuring period, the sun-exposed ground sidewalk is generally warmer and drier than the shaded elevated walkway, with a 0.4−1.5 ˚C higher T_a, a 7.6−12.6 ˚C higher T_g, and a 0.7−6.0 % lower RH. The v difference between the two sites ranges from -0.7 m/s to 0.8 m/s. The detailed comparison of meteorological parameters between the ground sidewalk and elevated walkway is described in Appendix B. Fig. 6(a) compares on-site measuring T_{mrt} between the ground sidewalk and elevated walkway. The range of T_{mrt} is 53.5−68.0 ˚C on the ground sidewalk and 19.9−39.6 ˚C on the elevated walkway. This result indicates that the elevated walkway has considerably lower T_{mrt} than the ground sidewalk. The disparity of T_{mrt}

between the two sites is 19.8−34.8 ˚C, more prominent in winter. Besides, the seasonal variation of T_{mrt} is 0.9−14.4 ˚C on the ground sidewalk and 14.3−19.7 ˚C on the elevated walkway throughout the measuring periods.

PET values based on measured meteorological parameters are depicted in Fig. 6(b). The ground-level PET values range from 45.8 ˚C to 51.1 ˚C in summer, indicating strong to extreme heat stresses on pedestrians (Fang et al., 2019; Lin and Matzarakis, 2008). In contrast, the walkway-level PET values vary between 32.6 ˚C and 37.3 ˚C, dropping by 10.9−17.3 ˚C. Therefore, in summer, pedestrians would feel "hot" to "very hot" on the ground sidewalk but "slightly warm" to "warm" on the elevated walkway, based on the relationship between PET and thermal sensation grade in humid subtropical climates (Fang et al., 2019; Huang et al., 2017; Lin and Matzarakis, 2008). In winter, the PET value declines to ~27.4 ˚C on the ground sidewalk and ~13.8 ˚C on the elevated walkway, which implies that pedestrians would perceive "neutral" to "slightly warm" on the ground sidewalk and "slightly cool" to "cool" on the elevated walkway (Fang et al., 2019; Huang et al., 2017; Lin and Matzarakis, 2008).

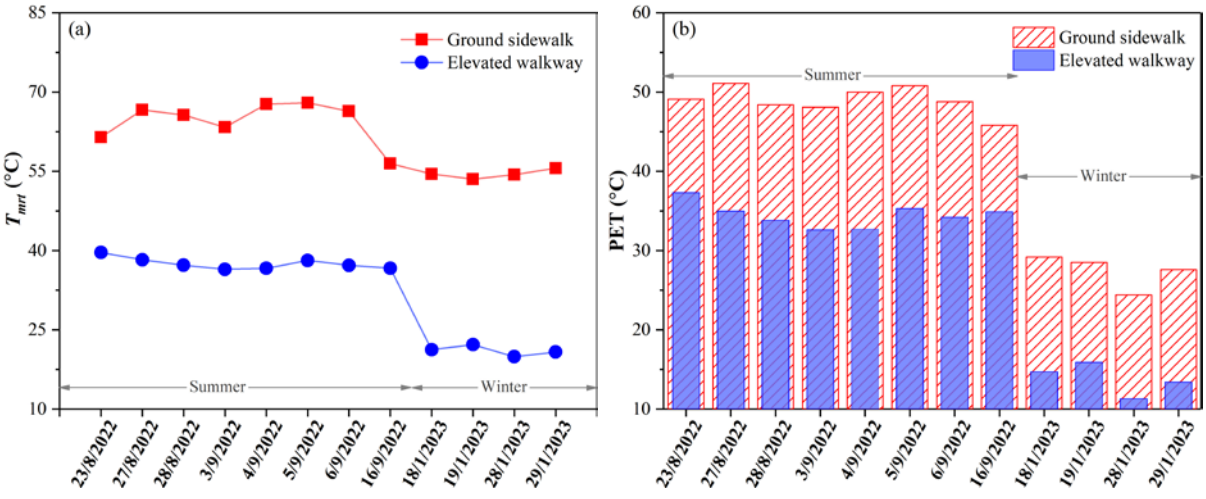

Fig. 6. (a) T_{mrt} and (b) PET at the ground sidewalk and elevated walkway sites during measuring periods.

3.2. Parametric simulation results based on ideal urban street canyons

3.2.1. Simulated results of *v* and SVF

Fig. 7 compares distributions of pedestrian-level *v* and SVF values on the windward sidewalk (WW), leeward sidewalk (LW), and elevated walkway (EW). The following lengths are described based on the prototype scale unless otherwise specified. This study sets thirty-one monitoring points to characterize the entire ground sidewalk or elevated walkway (30 m long). The interval between adjacent monitoring points is 1 m. All monitoring points are at the pedestrian level, 1.5 m above the ground or walkway floor. The WW and LW points are 2 m from the nearest building, while the EW points are in the middle of the elevated walkway. *H/W* = 1* is the basic elevated walkway case with *H/W* = 1, W_{ew} = 8 m, and OP-Wall. Other walkway cases are named according to their changes to the basic case.

Fig. 7(a) shows that *v* fluctuates obviously along the ground sidewalk or elevated walkway. Regarding the mean and median *v*, the ground-level *v* decreases remarkably after adding an 8m-wide elevated walkway in cases of *H/W* = 1, 2, and 3; EW has a higher *v* than WW and LW for five walkway cases with open sidewalls; ground-level and walkway-level *v* in walkway cases decrease first and then increase with rising *H/W*, while the values continuously decrease with increasing W_{ew}; case SH-Wall and case H-Wall have higher ground-level *v* than case OP-Wall (i.e., *H/W* = 1*), while case SH-Wall causes significantly lower walkway-level *v* than case OP-Wall. As case H-Wall is hermetic, this study does not discuss its walkway-level *v*.

Fig. 7(b) indicates that walkway cases always have lower ground-level SVF values than no-walkway cases due to the extra shelter from elevated walkways. In walkway cases, EW has much lower SVF values than LW and WW. The ground-level SVF values decline as *H/W* grows. In contrast, the walkway-level SVF values remain almost unchanged with *H/W*. Besides, when W_{ew} widens from 4 m to 12 m, the ground-level and walkway-level SVF values decrease. By comparing case OP-Wall, case SH-Wall, and case H-Wall, it can be found that the SVF values vary little with sidewall types.

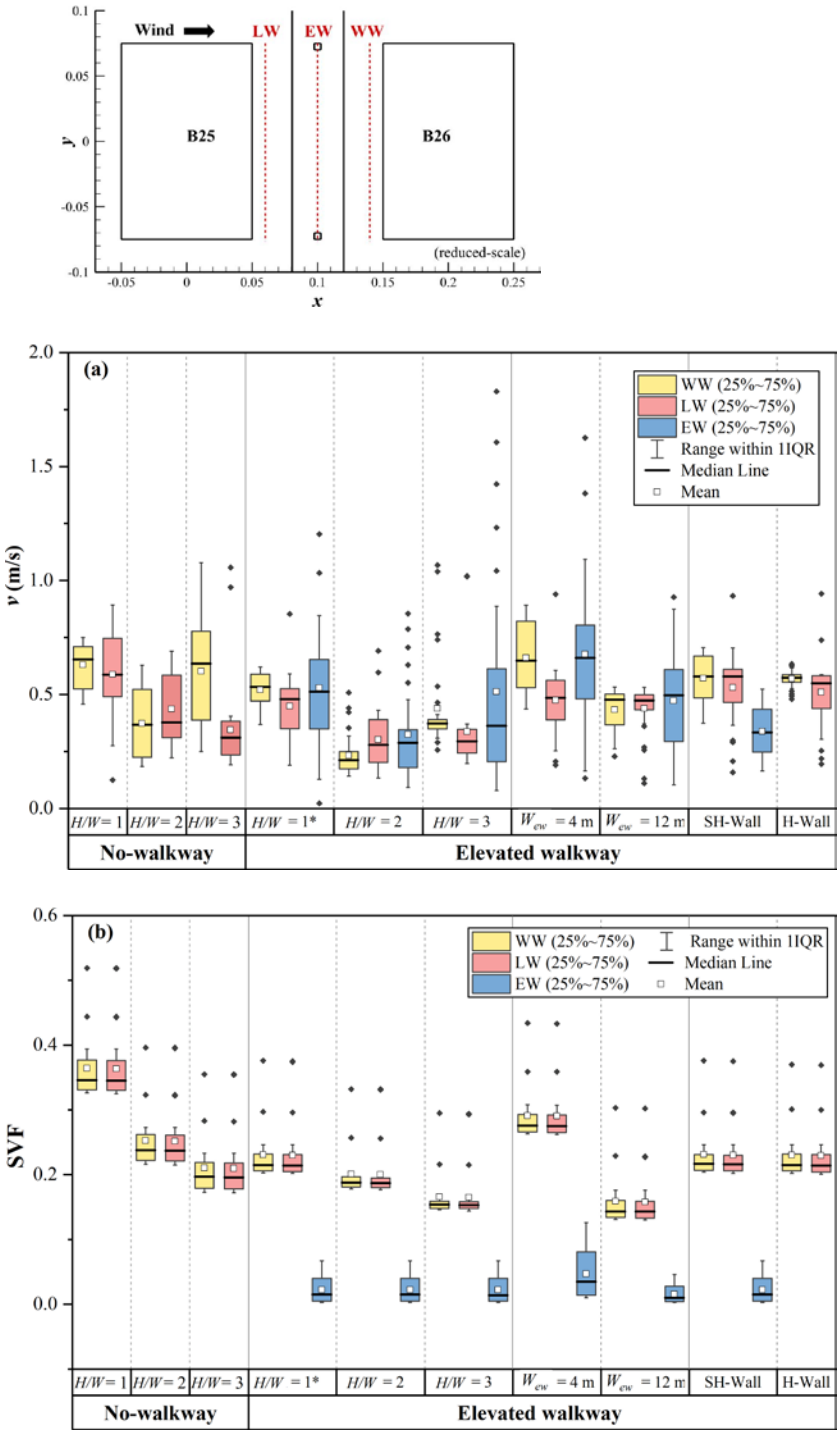

Fig. 7. Pedestrian-level (a) *v* and (b) SVF values on the ground sidewalk and elevated walkway for different modeling cases. The box charts present a 25−75% range of the data (box), the range within IQR (whisker), the median line (solid black line), the mean value (hollow square), and outliers (solid diamond).

3.2.2. Comparison of simulated T_{mrt} and PET between no-walkway and walkway cases

Fig. 8 compares pedestrian-level T_{mrt} and PET distributions on the ground sidewalk and elevated walkway between no-walkway and walkway cases. For three walkway cases, the walkway is 8 m wide and has open sidewalls. As shown in Fig. 8(a), the range of ground-level T_{mrt} is 56.9−61.3 ˚C for no-walkway cases and 57−61.9 ˚C for walkway cases in summer. Fig. 8(c) illustrates that the ground-level T_{mrt} is 42.6−48 ˚C for no-walkway cases and 43.5−48.6 ˚C for walkway cases in winter. The slight T_{mrt} difference between LW and WW can be observed for all cases. Concerning the box, mean value, and median line in Fig.8(a, c), walkway cases have higher ground-level T_{mrt} than no-walkway cases of identical *H/W*. Furthermore, the walkway-level T_{mrt} is 51.7−53.1 ˚C in summer and 38.1−39.7 in winter, indicating that the elevated walkway exhibits a significantly lower T_{mrt} than the ground sidewalk.

The PET box charts show similar characteristics to T_{mrt} box charts. Fig. 8(b, d) presents that the ground-level PET values are 43.0−49.6 ˚C in summer and 24.8−34.4 ˚C in winter in no-walkway cases. In contrast, walkway cases increase ground-level mean PET values by 0.1−1.3 ˚C in summer and 0.3−2.0 ˚C in winter. Furthermore, for walkway cases, the range of walkway-level PET values is 38.0−45.8 ˚C in summer and 19.3−32.3 ˚C in winter. The above results demonstrate that the elevated walkway results in 4.4−5.8 ˚C lower mean PET values in summer and 3.9−6.0 ˚C lower mean PET values in winter than the ground sidewalk.

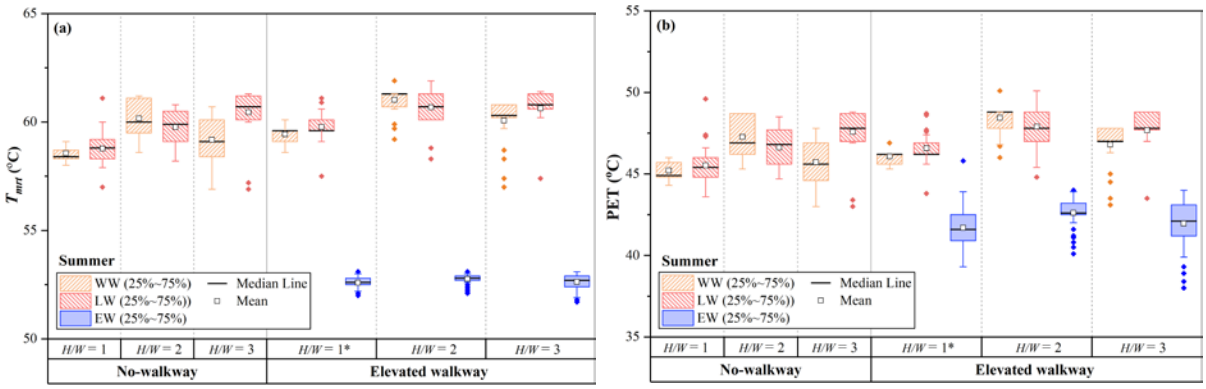

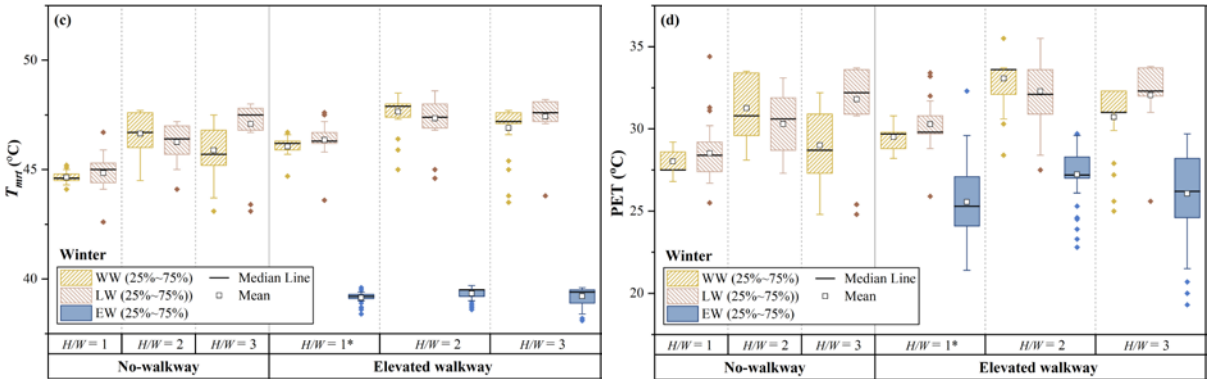

Fig. 8. Distributions of pedestrian-level T_{mrt} and PET values on the ground sidewalk (WW and LW) and elevated walkway (EW) in summer and winter in no-walkway and walkway cases with different *H/W* values.

3.2.3. Comparison of simulated T_{mrt} and PET between different street aspect ratios

Besides comparisons between no-walkway and walkway cases, Fig. 8 compares pedestrian-level T_{mrt} and PET values under different street aspect ratios (*H/W* = 1, 2, 3). Concerning walkway cases in summer, with *H/W* rising from 1 to 2, mean T_{mrt} values on WW, EW, and LW increase by ~1.6 ℃, ~0.2 ℃, and ~0.9℃; mean PET values on WW, EW, and LW increase by ~2.4 ℃, ~0.9 ℃, and ~1.3℃. The increments in mean T_{mrt} and PET values are more significant in winter than in summer. However, mean T_{mrt} and PET values on WW and EW decrease when *H/W* varies from 2 to 3. In contrast to WW and EW, mean T_{mrt} and PET values on LW vary little, below 0.1 ℃ and 0.3 ℃, respectively. Regarding no-walkway cases, the mean T_{mrt} and PET values on WW increase first and then decrease with *H/W,* while the values on LW rise continuously with *H/W*.

3.2.4. Comparison of simulated T_{mrt} and PET between different walkway widths

Pedestrian-level T_{mrt} and PET distributions on the ground sidewalk and elevated walkway under three walkway widths (W_{ew} = 4 m, 8m, 12 m) are depicted in Fig. 9. All cases are built with *H/W* = 1 and open sidewalls. Similar to the basic case of W_{ew} = 8 m, cases of W_{ew} = 4 m and 12 m have lower T_{mrt} and PET values on the elevated walkway than on the ground sidewalk.

This finding reinforces that the elevated walkway can reduce thermal comfort indices. Besides, the differences in T_{mrt} and PET values between WW and LW are pronounced when W_{ew} = 4 m, gradually diminishing as W_{ew} increases.

As illustrated in Fig. 9(a, c), whether on LW, WW, or EW, the mean T_{mrt} shows a rising trend as the walkway widens. Specifically, when the walkway broadens from 4 m to 12 m, the mean T_{mrt} on WW, LW, and EW increase by nearly 1.4 ˚C, 0.5 ˚C, and 0.3 ˚C in summer and 1.9 ˚C, 1.1 ˚C, and 0.4 ˚C in winter. Likewise, Fig. 9(b, d) demonstrates that the broadening of the walkway causes increased PET values. The maximum increase regarding the mean value of PET occurs on WW, with an increment of ~1.7 ˚C in summer and ~2.6 ˚C in winter, as the walkway widens from 4 m to 12 m. For EW, the mean value of PET increases by ~0.8 ˚C in summer and ~1.5 ˚C in winter when W_{ew} triples. In contrast to WW and EW, LW experiences the slightest increase in PET values due to the widening walkway. The increment is only ~0.5 ˚C in summer and ~0.8 ˚C in winter.

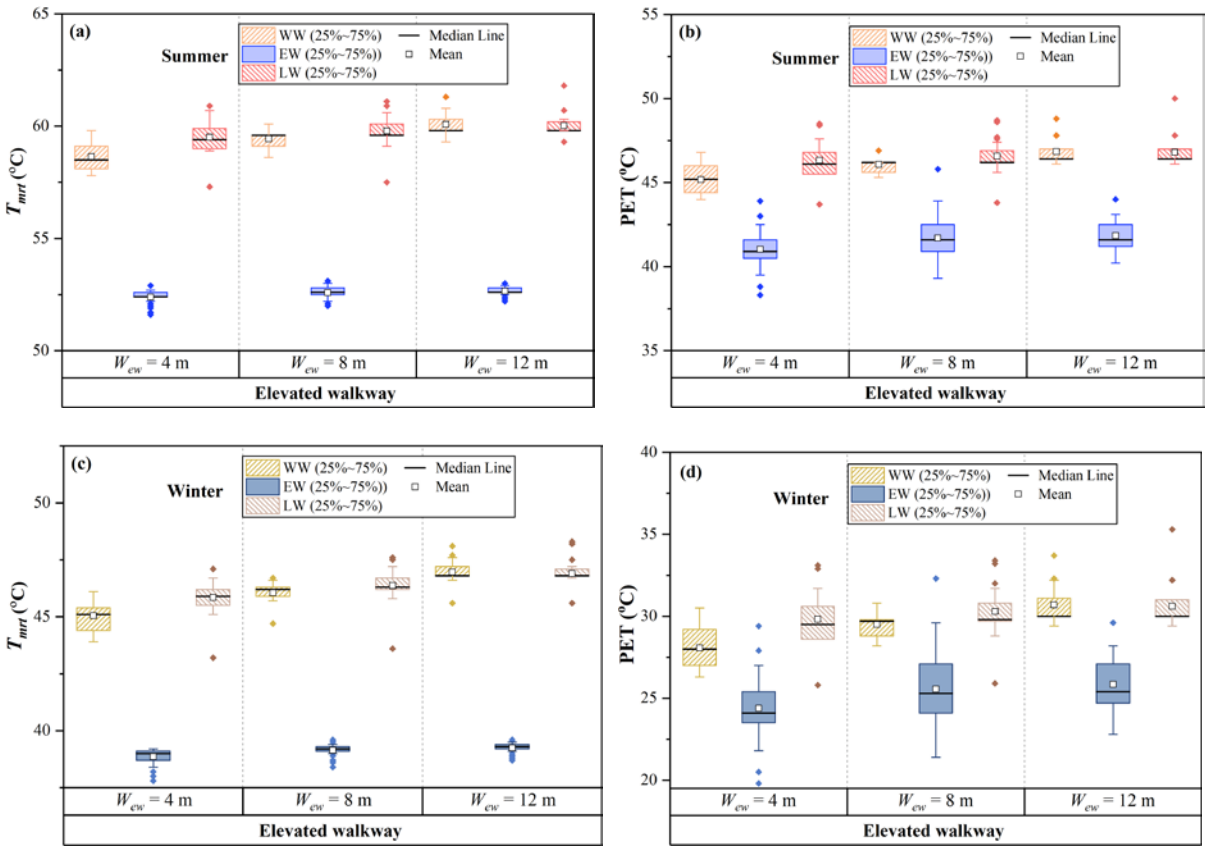

Fig. 9. Pedestrian-level distributions of T_{mrt} and PET on the ground sidewalk (WW and LW) and elevated walkway (EW) in summer and winter under different W_{ew}.

3.2.5. Comparison of simulated T_{mrt} and PET between different sidewall types

Fig. 10 compares pedestrian-level T_{mrt} and PET distributions on the ground sidewalk and elevated walkway in summer and winter among three walkway sidewall types. The three cases have the same H/W = 1 and W_{ew} = 8 m. As case H-Wall has a hermetic walkway, this study does not discuss outdoor thermal comfort on its elevated walkway. Fig. 10(a, c) shows that case SH-Wall has comparable ground-level mean T_{mrt} to case H-Wall. Moreover, the ground-level mean T_{mrt} declines in case SH-Wall and case H-Wall compared to case O-Wall, with a maximum reduction of 0.4 ˚C. The contrary result exists on the walkway-level mean T_{mrt}, as case SH-Wall has a slightly higher value than case O-Wall.

Fig. 10(b, d) illustrates that the distribution characteristics of PET among three sidewall types are similar to those of T_{mrt}. The ground-level mean PET value difference is insignificant between case SH-Wall and case H-Wall, within 0.1 ˚C. Moreover, case SH-Wall and case H-Wall have slightly lower ground-level PET values than case O-Wall. Specifically, the sidewalls decrease the mean value of PET on WW and LW by up to 0.4 ˚C and 0.5 ˚C in summer and 0.6 ˚C and 0.8 ˚C in winter, respectively. On the other hand, comparing case O-Wall with case SH-Wall, it can be observed that case SH-Wall results in a 0.7 ˚C and 1.3 ˚C drop in the mean value of walkway-level PET in summer and winter, respectively.

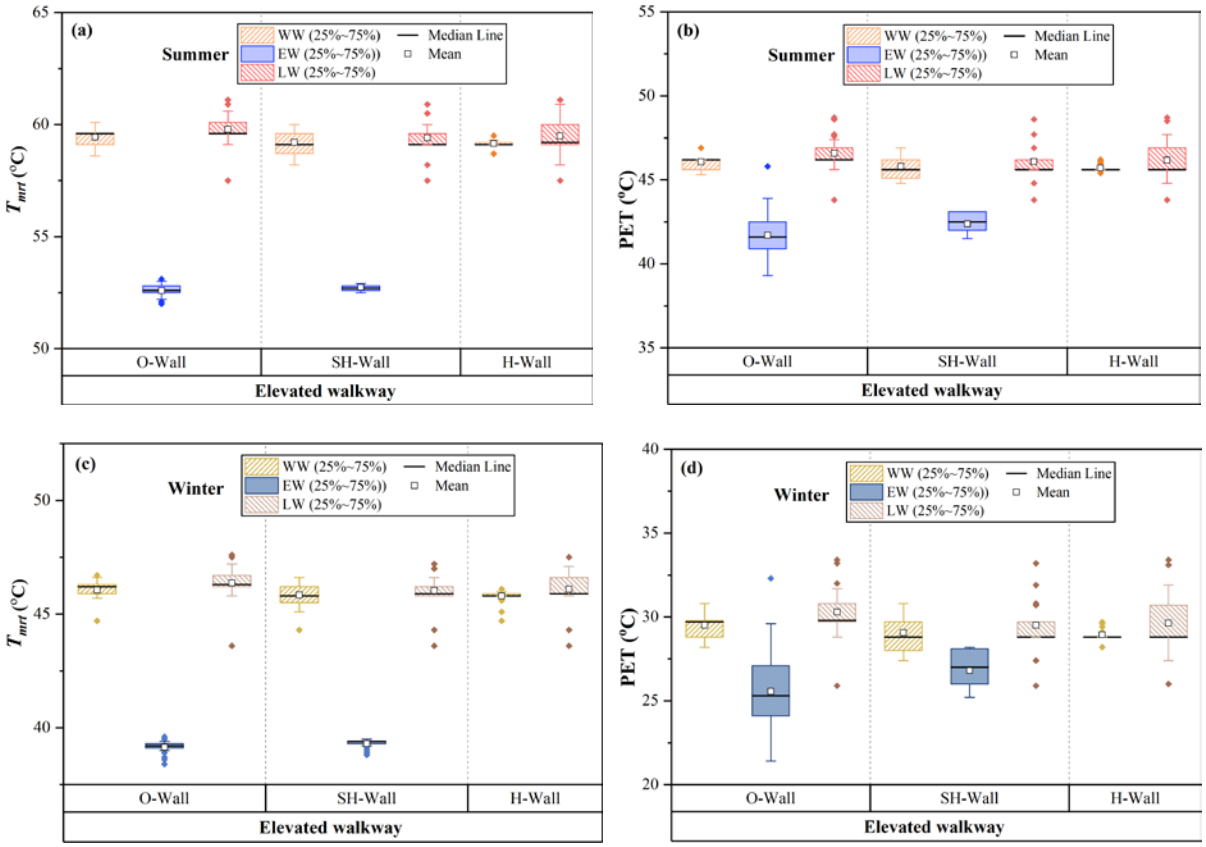

Fig. 10. Pedestrian-level distributions of T_{mrt} and PET on the ground sidewalk (LW and WW) and elevated walkway (WW) in summer and winter under three walkway sidewall types.

4. Discussion

4.1. Impacts of elevated walkways on the microclimate

The elevated walkway has a minor impact on daytime T_a and RH. The on-site measurements demonstrate that the covered elevated walkway can lead to a 0.4−1.5 ˚C reduction in T_a on sunny days (see Table B.1), aligning with previous studies on other shading strategies. For example, in Hong Kong, Huang et al. (2017) recorded a 0−2 ˚C reduction in T_a underneath an elevated building, and Lee et al. (2020) measured a maximum 0.8 ˚C cooling effect on T_a by the tinted glass cover in a ground walkway. In contrast to T_a, RH on the elevated walkway experiences a slight increase. RH is the percentage of the actual moisture content relative to the saturation moisture at the current temperature. Thus, the cool air with a lower saturation moisture has a higher RH than the warm air at the same actual moisture content,

which can partly explain the increase of RH on the elevated walkway. Niu et al. (2015) and Huang et al. (2017) measured a similar rise in daytime RH underneath elevated buildings in Hong Kong.

Unlike T_a and RH, the measured v difference between the ground sidewalk and elevated walkway is unstable. This phenomenon results from changeable wind directions and non-uniformly distributed obstacles (see Fig. 3(b)). Under the steady perpendicular wind, the spatial heterogeneity of simulated v is observed on the elevated walkway and ground sidewalk in ideal urban street canyons. In other words, some walkway positions have higher v than sidewalk positions, while others have lower or equivalent ones. On the other hand, from an overall perspective, the walkway-level v is slightly higher than the ground-level v in open sidewall conditions, more significant in deep street canyons. However, in the semi-hermetic sidewall condition, the walkway-level v is notably lower than the ground-level v due to the wind-blocking effect of sidewalls. Besides, the ground-level v generally decreases in the elevated walkway scenarios compared to no-walkway ones. This finding is consistent with the previous study on the entire street's pedestrian-level wind environment (Chen et al., 2023).

The elevated walkway experiences a considerable drop in daytime T_{mrt} compared to the ground sidewalk. The reduction in measured T_{mrt} can reach ~20−35 ˚C in high-rise LCZs, conforming to results in the literature regarding shading strategies. For example, Lam et al. (2023) reported that T_{mrt} decreases by up to 24.7 ˚C under opaque shading devices in a humid subtropical climate; Nasrollahi et al. (2021) discovered that the T_{mrt} difference between the shaded and sun-exposed sites reaches 34.2 ˚C in a hot desert climate. In ideal urban street canyons, the elevated walkway has a ~6−8 ˚C lower T_{mrt} than the ground sidewalk, depending upon the walkway dimension and street morphology. The simulated T_{mrt} difference between the ground sidewalk and elevated walkway is less apparent than on-site measurements. This phenomenon may be because the RayMan model underestimates T_{mrt} on the sun-exposed

sidewalk but overestimates the value on the shaded walkway (Lee and Mayer, 2016; Matzarakis, 2010). On the other hand, the elevated walkway causes a slight increase in the ground-level T_{mrt} in comparison to no-walkway scenarios. This finding can be ascribed to wind attenuation outweighing the reduction in SVF.

To sum up, among the four meteorological parameters influencing thermal comfort (T_a, v, RH, and T_{mrt}), the elevated walkway has the most significant effect on T_{mrt}.

4.2. Impacts of elevated walkways on outdoor thermal comfort

The elevated walkway can intercept a considerable amount of solar radiation during the daytime, so it has a substantially lower PET value than the ground sun-exposed sidewalk. On-site measurements show that the elevated walkway decreases PET by ~11−17 ˚C in high-rise LCZs, while simulated results indicate a PET reduction of ~2−6 ˚C by the elevated walkway in ideal urban street canyons of H/W = 1, 2, 3. The cooling effect of the elevated walkway on PET is comparable to that of other shading strategies (Lam et al., 2023; Lee et al., 2020; Nasrollahi et al., 2021). Additionally, comparing two types of urban street canyons, it can be found that elevated walkway scenarios cause up to 1.6 ˚C (2.7 ˚C) higher ground-level mean PET values than no-walkway scenarios in summer (winter)—such a heating effect on PET results from the weakened v on the ground sidewalk. Overall, although building an elevated walkway increases the ground-level PET value slightly, the elevated walkway provides a significantly lower walkway-level PET value.

It is worth noting that our results are based on the premise that the elevated walkway has an opaque cover. Other types of elevated walkways may exhibit a contrary conclusion. Yang et al. (2016) reported that the sun-exposed or steel-glass elevated walkway causes a higher PET value (i.e., worse thermal comfort) than the shaded ground sidewalk in summer. Furthermore, the materials and properties of shading devices influence thermal comfort significantly. Lam et

al. (2023) documented that opaque materials such as concrete, aluminum, and PVC have a superior cooling effect on PET than glass, and decreasing the glass transparency can enhance this cooling effect. Therefore, it can be deduced that the impact of the elevated walkway on thermal comfort is also subject to the materials and properties of the walkway's cover.

In summary, our results confirm that the elevated walkway with an opaque cover can effectively reduce PET, sequentially ameliorating pedestrian thermal comfort on hot days. Outdoor thermal comfort improvement is vital in hot-humid climate regions. A thermally comfortable environment gains people's interest and positivity in outdoor activities, thus reducing the duration of stay indoors (Niu et al., 2022). The sequential benefit is a reduction in cooling energy consumption from indoor air-conditioners.

4.3. Impacts of street aspect ratios (*H/W*) on outdoor thermal comfort

Parametric simulation results demonstrate that the walkway-level and ground-level PET values exhibit an initial increase and sequential decrease with rising *H/W* in ideal urban street canyons (see Fig. 8). As T_a, RH, and personal information are constant across different modeling cases in this study, the effects of *H/W* on PET are determined by the integrated impacts of wind velocity and thermal radiation. Deep street canyons with high *H/W* values generally result in lower SVF values, thus intercepting more solar radiation than shallow street canyons. On the other hand, deep street canyons have more solid surfaces, contributing to more intense long-wave radiation. Furthermore, *v* in deep street canyons may decrease due to an enhanced building-blocking effect or increase by a strengthened venturi effect. In this study, the ground-level SVF value decreases as *H/W* grows. However, the walkway-level SVF value varies negligibly with *H/W* because the elevated walkway is well-shaded. The walkway-level and ground-level *v* decline first and then improve as *H/W* increases from 1 to 3, opposite to the change of PET. Therefore, it can be concluded that *v* contributes most to the PET variation with *H/W*.

4.4. Impacts of walkway dimensions on outdoor thermal comfort

The positive correlation between PET and W_{ew} in ideal urban street canyons is confirmed in this study (see Fig. 9). Moreover, the impact of W_{ew} on PET is more significant on the elevated walkway and windward ground sidewalk and less evident for the leeward ground sidewalk. The PET variation due to W_{ew} is more prominent in winter than in summer. When the elevated walkway becomes wide (e.g., W_{ew} = 12 m), it blocks more entrained wind flows from the roof and pedestrians' view of the sky. Consequently, SVF and *v* at the pedestrian level show inverse relationships with W_{ew}. When the SVF value decreases, pedestrians generally receive less solar radiation but more long-wave radiation emitted from solid surfaces. Besides, low *v* tends to cause higher surface temperatures and thermal comfort indices than high *v* under the same external conditions. In this study, PET is increased under the wide walkway of W_{ew} = 12 m compared to the narrow walkway of W_{ew} = 4 m. Thus, the impacts of lower *v* and higher solid surfaces' long-wave radiation exceed the reduction in solar radiation.

The sidewall type has a negligible effect on pedestrian-level SVF values of the ground sidewalk and elevated walkway. Nevertheless, the pedestrian-level *v* varies under different sidewalls. The semi-hermetic and hermetic sidewalls increase ground-level *v* compared to the open sidewall. Therefore, the ground-level PET value is slightly lower in semi-hermetic and hermetic sidewalls than in the open sidewall (see Fig. 10). Furthermore, the semi-hermetic sidewall decreases the walkway-level *v* compared to the open sidewall, resulting in a high PET value on the elevated walkway. Regarding the hermetic sidewall, mechanical ventilation and air conditioning can help achieve thermal comfort on the elevated walkway.

4.5. Elevated walkway design implications

This study demonstrates that the elevated walkway with an opaque cover yields notably lower PET values than the sun-exposed ground sidewalk. Some implications for applying elevated walkways to urban design can be obtained from the perspective of thermal comfort.

In hot-humid cities like Hong Kong, adding an opaque cover to elevated walkways is crucial to mitigate pedestrian heat stress and improve pedestrian thermal comfort. This design is particularly significant in open LCZs and east-west oriented streets with limited shade from the buildings and trees. Moreover, open sidewalls like railings (see Fig. 1(a)) exhibit superior performance for reducing walkway-level heat stress than semi-hermetic sidewalls (see Fig. 1(b)). From economic and energy-saving perspectives, hermetic sidewalls (see Fig. 1(c)) requiring mechanical ventilation are unnecessary. Since the ground-level PET values increase due to elevated walkways, incorporating elevated building design, arcades, trees, and awnings into the adjacent buildings and ground sidewalks shall be an effective strategy to compensate for ground-level thermal comfort. In well-shaded deep street canyons with high *H/W*, the extra shading benefit of the opaque cover is limited. In this case, the opaque cover changes to be optional for elevated walkways. Removing cover may augment ground-level and walkway-level wind velocities and benefit thermal comfort, which requires further evidence. In places with hot-humid summers and cold winters, elevated walkways are appropriate for installing partial-shaded or adjustable covers. These covers either divide the walkway into sunny and shaded zones or provide shade in summer and allow sunlight penetration in winter.

4.6. Limitations and future work

First, despite being a typical parallel footbridge in a busy district, the measured elevated walkway cannot thoroughly characterize the wide variety of elevated walkways in Hong Kong. Further on-site measurements are necessary to heighten the knowledge of elevated walkways with diverse forms and surrounding geometries. Moreover, on-site measurements were alternated between the elevated walkway and ground sidewalk sites, which could eliminate the influence of equipment. Nevertheless, since meteorological parameters are dynamic, alternate measurements may miss some simultaneous meteorological variations occurring at both sites, introducing disturbances to observed differences between the two sites.

Second, the scope of this study is limited to sunny weather conditions and specific periods (i.e., exposure to direct sunlight). The thermal comfort difference between the ground sidewalk and elevated walkway may change in cloudy weather or when the surroundings shade the ground sidewalk. Future research can include different weather conditions, periods, and seasons. Third, the elevated walkway's cooling effect on T_{mrt} and PET may be unfavorable in temperate and cold climate regions, where the elevated walkway is more appropriate to have a transparent cover (e.g., a glass canopy) or be hermetic. More investigations are worthwhile to determine the optimal walkways appropriate for different climates.

Fourth, the parametric simulation study was based on the parallel elevated walkway and the ideal urban street canyon models with identical building blocks and perpendicular wind. The impacts of street aspect ratio and walkway dimensions on outdoor thermal comfort may differ under other walkway orientations (e.g., perpendicular elevated walkways), urban geometries (e.g., staggered, random-distributed, and uneven building arrays), and wind directions. Furthermore, in authentic street environments, street trees and building overhangs can influence pedestrian thermal comfort, which deserves consideration in future research. Last, this study only used PET to assess outdoor thermal comfort. However, PET cannot thoroughly explain pedestrian thermal perception, which is also influenced by physiological, psychological, behavioral, personal, social, cultural, thermal history, alliesthesia, and other factors (Lai et al., 2020). Future work will introduce questionnaire surveys to examine subjective satisfaction with the thermal environment on the elevated walkway and explore the impacts of other non-physical factors.

5. Conclusions

This study evaluated outdoor thermal comfort on the ground sidewalk and elevated walkway under different conditions. On-site measurements were conducted on the section of Cheong Wan Road footbridge in Hong Kong. LES and RayMan modeling were used to

examine the effects of walkway dimensions and street aspect ratio on outdoor thermal comfort in ideal urban street canyons. The main findings are summarized below:

(1). T_{mrt} and PET decrease substantially on the elevated walkway compared to the ground sidewalk, up to 34.8 ˚C and 17.3 ˚C in an authentic street environment. However, the elevated walkway's cooling effect on T_a is minor, within 1.5 ˚C.

(2). The elevated walkway decreases ground-level SVF and *v* in ideal urban street canyons. As a result, the ground-level T_{mrt} and PET values are increased slightly after adding an elevated walkway. These variations become prominent as the elevated walkway widens.

(3). In ideal urban street canyons, ground-level and walkway-level PET values increase initially and sequentially decrease with an increase in *H/W* from 1 to 3, while they positively correlate with W_{ew}. Compared to the open sidewall, the semi-hermetic sidewall has a maximum 0.8 ˚C lower ground-level PET value but a maximum 1.3 ˚C higher walkway-level PET value.

This study bridges the research gap between covered elevated walkways and outdoor thermal comfort and contributes to understanding the impacts of elevated walkway dimensions and street aspect ratio on pedestrian thermal comfort. Our findings confirm that the elevated walkway with an opaque cover can substantially improve pedestrian thermal comfort by providing shade in hot and humid regions, where thermal discomfort is primarily due to intense heat stress. Helpful recommendations have been provided for urban planners in the applications of elevated walkways in hot-humid cities.

Appendix A

Table A.1 Monthly averages of daily maximum (T_{max}, ℃), mean (T_a, ℃), and minimum (T_{min}, ℃) temperatures, relative humidity (RH) at 14: 00 hours, rainfall (mm), prevailing wind direction (θ, °), and wind velocity (v, m/s) (Hong Kong Observatory, n.d.-b).

	Hong Kong Observatory (urban area)												
Month	Jan	Feb	Mar	Apr	May	Jun	Jul	Aug	Sep	Oct	Nov	Dec	Year
T_{max}	18.7	19.4	21.9	25.6	28.8	30.7	31.6	31.3	30.5	28.1	24.5	20.4	26.0
T_a	16.5	17.1	19.5	23.0	26.3	28.3	28.9	28.7	27.9	25.7	22.2	18.2	23.5
T_{min}	14.6	15.3	17.6	21.1	24.5	26.5	26.9	26.7	26.1	23.9	20.3	16.2	21.6
RH	67	72	75	75	76	76	74	74	71	65	65	63	71
Rainfall	33.2	38.9	75.3	153.0	290.6	491.5	385.8	453.2	321.4	120.3	39.3	28.8	2431.2
θ	90	90	90	90	90	260	260	260	90	90	90	90	90
v	2.6	3.0	3.1	2.7	2.6	2.6	2.8	2.5	2.8	2.9	2.8	2.6	2.8
	Waglan Island (rural area)												
θ	60	60	60	70	80	220	230	230	80	80	70	10	70
v	7.0	6.7	6.4	5.7	5.5	6.0	5.9	5.2	5.9	7.3	7.4	7.3	6.4

Appendix B Meteorological parameters

Table B.1 enumerates on-site measured meteorological data during various measuring periods. The data per experiment date resulted from averaging all rounds of samples. For convenience, although each place had two measuring sites, the data were classified according to site type (SW, EW) instead of the specific position (S1, S2, E1, E2). Table B.1 indicates that four meteorological parameters differ between the two sites. Significant seasonal variations in T_a and T_g can be observed by comparing summer and winter data. During the measuring period, the sun-exposed ground sidewalk is generally warmer and drier than the shaded elevated walkway, with a 0.4−1.5 ˚C higher T_a, a 7.6−12.6 ˚C higher T_g, and a 0.7−6.0 % lower RH. The v difference between the two sites ranges from -0.7 m/s to 0.8 m/s, indicating that the elevated walkway is not necessarily windier than the ground sidewalk. The above results provide preliminary evidence of the elevated walkway's shading/cooling effects on radiation/air temperature.

Table B.1 Summary of T_a, RH, v, and T_g recorded at ground sidewalk (SW) and elevated walkway (EW) sites during on-site measuring periods.

Season	Date	T_a (°C)		RH (%)		v (m/s)		T_g (°C)	
	(dd/mm/yyyy)	SW	EW	SW	EW	SW	EW	SW	EW
Summer	23/08/2022	35.5	34.3	55.3	61.3	1.0	0.8	44.9	36.4
	27/08/2022	33.7	32.6	57.8	60.5	0.8	0.9	47.2	34.6
	28/08/2022	33.1	32.0	66.5	70.2	1.5	1.3	42.9	33.6
	03/09/2022	33.0	32.0	40.3	42.5	1.0	1.7	44.0	33.2
	04/09/2022	33.1	32.1	43.6	45.7	1.2	2.0	44.6	33.3
	05/09/2022	34.3	33.5	36.2	37.3	1.4	1.0	44.9	35.2
	06/09/2022	33.6	32.7	40.3	42.6	1.7	1.0	43.1	34.3
	16/09/2022	34.9	33.4	45.7	50.5	1.1	0.9	42.3	34.7
Winter	18/01/2023	17.9	16.5	44.3	47.0	1.1	0.9	28.9	17.5
	19/01/2023	18.9	18.0	51.0	52.8	1.4	1	28.5	18.9
	28/01/2023	15.0	14.0	15.4	16.1	1.5	1.2	25.2	15.1
	29/01/2023	15.5	15.1	21.1	22.2	1.1	0.8	27.5	16.3

References

Ai Z. T., and Mak C. M. 2015. Large-eddy Simulation of flow and dispersion around an isolated building: Analysis of influencing factors. *Computers & Fluids, 118,* 89-100. https://doi.org/10.1016/j.compfluid.2015.06.006.

Aleksandrowicz O., and Pearlmutter D. 2023. The significance of shade provision in reducing street-level summer heat stress in a hot Mediterranean climate. *Landscape and Urban Planning, 229*. https://doi.org/10.1016/j.landurbplan.2022.104588.

Ali-Toudert F., and Mayer H. 2007. Effects of asymmetry, galleries, overhanging façades and vegetation on thermal comfort in urban street canyons. *Solar Energy, 81*(6), 742-754. https://doi.org/10.1016/j.solener.2006.10.007.

ANSYS Fluent 19.0. 2018. *ANSYS Fluent User's Guide*. Canonsburg, PA.

ASHRAE. 2013. ASHRAE Standard 55: Thermal Environmental Conditions for Human Occupancy. In (pp. 54): ASHRAE.

ASHRAE. 2017. *ASHRAE Fundamentals Handbook 2017 (SI Edition)*: American Society of Heating Refrigerating and Air-Conditioning Engineers Inc.

C3S. 2022. Copernicus: Summer 2022 Europe's hottest on record [Press release]. Retrieved from https://climate.copernicus.eu/copernicus-summer-2022-europes-hottest-record

Chen L., Mak C. M., Hang J., et al. 2023. Large eddy simulation study on pedestrian-level wind environments around elevated walkways and influential factors in ideal urban street canyons. *Building and Environment, 235*, 110236. https://doi.org/10.1016/j.buildenv.2023.110236.

Cheung P. K., and Jim C. Y. 2018. Comparing the cooling effects of a tree and a concrete shelter using PET and UTCI. *Building and Environment, 130*, 49-61. https://doi.org/10.1016/j.buildenv.2017.12.013.

Crewe K., Brazel A., and Middel A. 2016. Desert New Urbanism: testing for comfort in downtown Tempe, Arizona. *Journal of Urban Design, 21*(6), 746-763. https://doi.org/10.1080/13574809.2016.1187558.

Dai Y., Mak C. M., Ai Z., et al. 2018. Evaluation of computational and physical parameters influencing CFD simulations of pollutant dispersion in building arrays. *Building and Environment, 137*, 90-107. https://doi.org/10.1016/j.buildenv.2018.04.005.

Du Y., Mak C. M., Huang T., et al. 2017. Towards an integrated method to assess effects of lift-up design on outdoor thermal comfort in Hong Kong. *Building and Environment, 125*, 261-272. https://doi.org/10.1016/j.buildenv.2017.09.001.

Duan G., Brimblecombe P., Chu Y. L., et al. 2020. Turbulent flow and dispersion inside and around elevated walkways. *Building and Environment, 173*, 106711. https://doi.org/10.1016/j.buildenv.2020.106711.

Elgheznawy D., and Eltarabily S. 2021. The impact of sun sail-shading strategy on the thermal comfort in school courtyards. *Building and Environment, 202*, 108046. https://doi.org/10.1016/j.buildenv.2021.108046.

Fang Z., Feng X., Xu X., et al. 2019. Investigation into outdoor thermal comfort conditions by different seasonal field surveys in China, Guangzhou. *International Journal of Biometeorology, 63*(10), 1357-1368. https://doi.org/10.1007/s00484-019-01752-8.

Fluent. 2013. ANSYS Fluent Theory Guide. In. Canonsburg, PA: ANSYS Inc.

Franke J., Hellsten A., Schlünzen H., et al. 2007. *Best practice guideline for the CFD simulation of flows in the urban environment: : COST Action 732 Quality Assurance and Improvement of Microscale Meteorological Models*. <Go to ISI>://WOS:000288567900048

Hanna S. R., Hansen O. R., and Dharmavaram S. 2004. FLACS CFD air quality model performance evaluation with Kit Fox, MUST, Prairie Grass, and EMU observations. *Atmospheric Environment, 38*(28), 4675-4687. https://doi.org/10.1016/j.atmosenv.2004.05.041.

Highways Department. 2022. *Footbridges and Subways of Hong Kong*. Retrieved from Hong Kong: https://www.hyd.gov.hk/en/information_corner/hyd_factsheets/doc/e_Footbridges_and_Subways.pdf

Hong Kong Observatory. (n.d.-a). Climatological Information Services: Daily Exact. Retrieved from https://www.hko.gov.hk/en/cis/climat.htm

Hong Kong Observatory. (n.d.-b). Monthly Meteorological Normals for Hong Kong (1991-2020). Retrieved from https://www.hko.gov.hk/en/cis/normal/1991_2020/normals.htm

Höppe P. 1992. A new method for determining the mean radiation temperature outdoors. *Wetter unt Leben, 44*, 147-151.

Höppe P. 1999. The physiological equivalent temperature - a universal index for the biometeorological assessment of the thermal environment. *International Journal of Biometeorology, 43*(2), 71-75. https://doi.org/10.1007/s004840050118.

Huang T., Li J., Xie Y., et al. 2017. Simultaneous environmental parameter monitoring and human subject survey regarding outdoor thermal comfort and its modelling. *Building and Environment, 125*, 502-514. https://doi.org/10.1016/j.buildenv.2017.09.015.

ISO 9920:2007. 2007. Ergonomics of the Thermal Environment — Estimation of Thermal Insulation and Water Vapour Resistance of a Clothing Ensemble. In. International Organization for Standardization, Geneva.

Jiang J., Liu Y., Mao J., et al. 2023. Extreme heatwave over Eastern China in summer 2022: the role of three oceans and local soil moisture feedback. *Environmental Research Letters, 18*(4), 044025. https://doi.org/10.1088/1748-9326/acc5fb.

Kántor N., Chen L., and Gál C. V. 2018. Human-biometeorological significance of shading in urban public spaces—Summertime measurements in Pécs, Hungary. *Landscape and Urban Planning, 170*, 241-255. https://doi.org/10.1016/j.landurbplan.2017.09.030.

Kántor N., Kovács A., and Lin T.-P. 2014. Looking for simple correction functions between the mean radiant temperature from the “standard black globe” and the “six-directional” techniques in Taiwan. *Theoretical and Applied Climatology, 121*(1-2), 99-111. https://doi.org/10.1007/s00704-014-1211-2.

Kottek M., J. Grieser, C. Beck, B. Rudolf, and F. Rubel. 2006. World Map of the Köppen-Geiger climate classification updated. *Meteorologische Zeitschrift, 15*, 259-263. https://doi.org/10.1127/0941-2948/2006/0130.

Kumar P., and Sharma A. 2020. Study on importance, procedure, and scope of outdoor thermal comfort –A review. *Sustainable Cities and Society, 61*. https://doi.org/10.1016/j.scs.2020.102297.

Lai D., Lian Z., Liu W., et al. 2020. A comprehensive review of thermal comfort studies in urban open spaces. *Science of the Total Environment, 742*, 140092. https://doi.org/10.1016/j.scitotenv.2020.140092.

Lai D., Liu W., Gan T., et al. 2019. A review of mitigating strategies to improve the thermal environment and thermal comfort in urban outdoor spaces. *Science of the Total Environment, 661*, 337-353. https://doi.org/10.1016/j.scitotenv.2019.01.062.

Lai D., Liu Y., Liao M., et al. 2023. Effects of different tree layouts on outdoor thermal comfort of green space in summer Shanghai. *Urban Climate, 47,* 101398. https://doi.org/10.1016/j.uclim.2022.101398.

Lam C. K. C., Hang J., Zhang D., et al. 2021. Effects of short-term physiological and psychological adaptation on summer thermal comfort of outdoor exercising people in China. *Building and Environment, 198,* 107877. https://doi.org/10.1016/j.buildenv.2021.107877.

Lam C. K. C., Weng J., Liu K., et al. 2023. The effects of shading devices on outdoor thermal and visual comfort in Southern China during summer. *Building and Environment, 228,* 109743. https://doi.org/10.1016/j.buildenv.2022.109743.

Lee H., and Mayer H. 2016. Validation of the mean radiant temperature simulated by the RayMan software in urban environments. *International Journal of Biometeorology, 60*(11), 1775-1785. https://doi.org/10.1007/s00484-016-1166-3.

Lee I., Voogt J., and Gillespie T. 2018. Analysis and Comparison of Shading Strategies to Increase Human Thermal Comfort in Urban Areas. *Atmosphere, 9*(3), 91. https://doi.org/10.3390/atmos9030091.

Lee L. S. H., Cheung P. K., Fung C. K. W., et al. 2020. Improving street walkability: Biometeorological assessment of artificial-partial shade structures in summer sunny conditions. *International Journal of Biometeorology, 64*(4), 547-560. https://doi.org/10.1007/s00484-019-01840-9.

Leitl B., and Schatzmann M. (2010). Flow and dispersion in a finite array of rectangular buildings. Retrieved from http://www.mi.uni-hamburg.de/cedval.2010

Li J., Niu J., Huang T., et al. 2022a. Dynamic effects of frequent step changes in outdoor microclimate environments on thermal sensation and dissatisfaction of pedestrian during summer. *Sustainable Cities and Society, 79,* 103670. https://doi.org/10.1016/j.scs.2022.103670.

Li J., Niu J., and Mak C. M. 2022b. Study of pedestrians' mixed thermal responses when experiencing rapid and simultaneous variations in sun and wind conditions in urban continuums. *Sustainable Cities and Society, 87,* 104169. https://doi.org/10.1016/j.scs.2022.104169.

Li Y., Hong B., Wang Y., et al. 2022c. Assessing heat stress relief measures to enhance outdoor thermal comfort: A field study in China's cold region. *Sustainable Cities and Society, 80,* 103813. https://doi.org/10.1016/j.scs.2022.103813.

Li Z., Zhang H., Juan Y.-H., et al. 2023. Effects of urban tree planting on thermal comfort and air quality in the street canyon in a subtropical climate. *Sustainable Cities and Society, 91,* 104334. https://doi.org/10.1016/j.scs.2022.104334.

Li Z., Zhang H., Wen C.-Y., et al. 2020. Effects of frontal area density on outdoor thermal comfort and air quality. *Building and Environment, 180*, 107028. https://doi.org/10.1016/j.buildenv.2020.107028.

Lin T.-P., Tsai K.-T., Liao C.-C., et al. 2013. Effects of thermal comfort and adaptation on park attendance regarding different shading levels and activity types. *Building and Environment, 59*, 599-611. https://doi.org/10.1016/j.buildenv.2012.10.005.

Lin T. P., and Matzarakis A. 2008. Tourism climate and thermal comfort in Sun Moon Lake, Taiwan. *International Journal of Biometeorology, 52*(4), 281-290. https://doi.org/10.1007/s00484-007-0122-7.

Mahmoud R. M. A., and Abdallah A. S. H. 2022. Assessment of outdoor shading strategies to improve outdoor thermal comfort in school courtyards in hot and arid climates. *Sustainable Cities and Society, 86*, 104147. https://doi.org/10.1016/j.scs.2022.104147.

Matzarakis A., and Matuschek O. 2011. Sky view factor as a parameter in applied climatology rapid estimation by the SkyHelios model. *Meteorologische Zeitschrift, 20*(1), 39-45. https://doi.org/10.1127/0941-2948/2011/0499.

Matzarakis A., Rutz, F., Mayer, H. 2007. Modelling Radiation fluxes in simple and complex environments – Application of the RayMan model. *International Journal of Biometeorology 51*, 12.

Matzarakis A., Rutz, F., Mayer, H. 2010. Modelling Radiation fluxes in simple and complex environments – Basics of the RayMan model. *International Journal of Biometeorology 54*, 9.

Middel A., AlKhaled S., Schneider F. A., et al. 2021. 50 Grades of Shade. *Bulletin of the American Meteorological Society, 102*(9), E1805-E1820. https://doi.org/10.1175/bams-d-20-0193.1.

Nasrollahi N., Namazi Y., and Taleghani M. 2021. The effect of urban shading and canyon geometry on outdoor thermal comfort in hot climates: A case study of Ahvaz, Iran. *Sustainable Cities and Society, 65*, 102638. https://doi.org/10.1016/j.scs.2020.102638.

Niu J., Hong B., Geng Y., et al. 2020. Summertime physiological and thermal responses among activity levels in campus outdoor spaces in a humid subtropical city. *Sci Total Environ, 728*, 138757. https://doi.org/10.1016/j.scitotenv.2020.138757.

Niu J., Liu J., Lee T.-c., et al. 2015. A new method to assess spatial variations of outdoor thermal comfort: Onsite monitoring results and implications for precinct planning. *Building and Environment, 91*, 263-270. https://doi.org/10.1016/j.buildenv.2015.02.017.

Niu J., Xiong J., Qin H., et al. 2022. Influence of thermal comfort of green spaces on physical activity: Empirical study in an urban park in Chongqing, China. *Building and Environment, 219*, 109168. https://doi.org/10.1016/j.buildenv.2022.109168.

Palomo Amores T. R., Sánchez Ramos J., Guerrero Delgado M., et al. 2023. Effect of green infrastructures supported by adaptative solar shading systems on livability in open spaces. *Urban Forestry & Urban Greening, 82*, 127886. https://doi.org/10.1016/j.ufug.2023.127886.

Perkins-Kirkpatrick S. E., and Lewis S. C. 2020. Increasing trends in regional heatwaves. *Nat Commun, 11*(1), 3357. https://doi.org/10.1038/s41467-020-16970-7.

Rossi F., Cardinali M., Di Giuseppe A., et al. 2022. Outdoor thermal comfort improvement with advanced solar awnings: Subjective and objective survey. *Building and Environment, 215*, 108967. https://doi.org/10.1016/j.buildenv.2022.108967.

Rotmeyer J. 2006. *Can elevated pedestrian walkways be sustainable?* Paper presented at the The Sustainable City IV: Urban Regeneration and Sustainability.

Sabatino S. D., Buccolieri R., Olesen H. R., et al. 2011. COST 732 in practice: the MUST model evaluation exercise. *International Journal of Environment and Pollution, 44*(1/2/3/4). https://doi.org/10.1504/ijep.2011.038442.

Schatzmann M O. H. R., Franke J 2010. *COST 732 Model Evaluation Case Studies: Approach and Results*. Brussels, Belgium: COST Office

Talebsafa S., Shahraeini M. T., Yang X. S., et al. 2023. Impact of Providing Shade on Outdoor Thermal Comfort during Hot Season: a Case Study of a University Campus in Cold Semi-arid Climate. *Renewable Energy Research and Applications, 4*(2), 209-224. https://doi.org/10.22044/rera.2022.12254.1169.

Tan Z., Wang A., Morakinyo T. E., et al. 2022. Assessing the mitigation performance of building setback from street and the combination with roadside tree planting. *Building and Environment, 212*, 108814. https://doi.org/10.1016/j.buildenv.2022.108814.

Tominaga Y., Mochida A., Yoshie R., et al. 2008. AIJ guidelines for practical applications of CFD to pedestrian wind environment around buildings. *Journal of Wind Engineering and Industrial Aerodynamics, 96*(10-11), 1749-1761. https://doi.org/10.1016/j.jweia.2008.02.058.

Watanabe S., Nagano K., Ishii J., et al. 2014. Evaluation of outdoor thermal comfort in sunlight, building shade, and pergola shade during summer in a humid subtropical region. *Building and Environment, 82*, 556-565. https://doi.org/10.1016/j.buildenv.2014.10.002.

Xu M., Hong B., Mi J., et al. 2018. Outdoor thermal comfort in an urban park during winter in cold regions of China. *Sustainable Cities and Society, 43*, 208-220. https://doi.org/10.1016/j.scs.2018.08.034.

Yang F., Qian F., and Zhao W. 2016. Towards a Climate-Responsive Vertical Pedestrian System: An Empirical Study on an Elevated Walkway in Shanghai China. *Sustainability, 8*(8), 744. https://doi.org/10.3390/su8080744.

Yang S. R., Lan S. T., Wu Y. T., et al. 2023. Applying expanded metal mesh for outdoor shades in outdoor thermal environments. *International Journal of Biometeorology*, 1-11. https://doi.org/10.1007/s00484-023-02494-4.

Yıldırım M. 2020. Shading in the outdoor environments of climate-friendly hot and dry historical streets: The passageways of Sanliurfa, Turkey. *Environmental Impact Assessment Review, 80*, 106318. https://doi.org/10.1016/j.eiar.2019.106318.

Yin S., Lang W., and Xiao Y. 2019. The synergistic effect of street canyons and neighbourhood layout design on pedestrian-level thermal comfort in hot-humid area of China. *Sustainable Cities and Society, 49*. https://doi.org/10.1016/j.scs.2019.101571.

Yin S., Wang F., Xiao Y., et al. 2022. Comparing cooling efficiency of shading strategies for pedestrian thermal comfort in street canyons of traditional shophouse neighbourhoods in Guangzhou, China. *Urban Climate, 43*, 101165. https://doi.org/10.1016/j.uclim.2022.101165.

Zheng Y., Ren C., Xu Y., et al. 2018. GIS-based mapping of Local Climate Zone in the high-density city of Hong Kong. *Urban Climate, 24*, 419-448. https://doi.org/10.1016/j.uclim.2017.05.008.

Zhong H., Feng J., Lam C. K. C., et al. 2023. The impact of semi-open street roofs on urban pollutant exposure and pedestrian-level thermal comfort in 2-D street canyons. *Building and Environment, 239*, 110387. https://doi.org/10.1016/j.buildenv.2023.110387.